J. COMBIN. MATH. COMBIN. COMPUT. 127a (2025) 5715--5746

Journal of Combinatorial Mathematics and Combinatorial Computing
www.combinatorialpress.com/jcmcc

Combinatorial Press

Optimization simulation and application of welding process of steel pipe in Dianzhong water diversion project based on variational method

Bo Gao[1,✉], Hengxin Jiang[1], Jianwei Xu[2], Yangguang Chen[3]

[1] *College of Science, Wuhan University of Technology, Wuhan, Hubei, 438300, China*

[2] *School of Mechanical and Electrical Engineering, East China Jiaotong University, Jiujiang, Jiangxi, 332004, China*

[3] *School of Mechanical Engineering, Lushan College of Guangxi University of Science and Technology, Liuzhou, Guangxi, 545000, China*

ABSTRACT

The mechanism study of steel pipe welding in Dianzhong water diversion project is very complicated, and there are many process parameters affecting the temperature distribution of high-frequency heating of welded steel pipe, and the degree of influence and the influence law are not the same. In this paper, Abaqus software is used to carry out the finite element analysis of the steel pipe welding process, and the displacement variational method (i.e., Ritz method) is introduced to derive the radial displacement of the steel pipe when it is subjected to the action of the centralized force, so as to realize the finite element simulation of the welding process of the steel pipe. At the same time, the optimization of the welding process parameters of the steel pipe is realized by combining the radial basis function neural network (RBF) and particle swarm algorithm (PSO). The simulation results show that the Von mise equivalent residual stress at the weld seam reaches the nominal yield strength of the material on both the internal and external surfaces of the steel pipe, while the axial residual stress has a very different distribution law on the internal and external walls of the steel pipe, which belongs to the tensile stress and weld residual compressive stress at the weld seams on the internal and external walls of the steel pipe, which are about 0.4 times the yield strength of the material and 0.7 times the yield strength of the material, respectively. The ring residual stress distribution law of the steel pipe is similar to the axial residual stress, but both reach the nominal yield strength of the material. Through parameter optimization, this paper determines that when the opening angle is 5°, the current frequency is 217.35 kHz, and the distance from the coil to the V-point is 252 mm, the corresponding optimization target values are all smaller, and the welding quality of the corresponding weld seam is better. The research in this paper provides a theoretical basis for further improving the welding quality of steel pipe in Dianzhong water diversion project.

✉ Corresponding author.
E-mail address: ztjq1522337@163.com (B. Gao).

Received 01 February 2024; Revised 20 April 2024; Accepted 10 November 2024; Published Online 15 April 2025.
DOI: 10.61091/jcmcc127a-318

Keywords: finite element analysis, steel pipe welding, variational method, RBF neural network, PSO algorithm

1. Introduction

Central Yunnan is located in the center of Yunnan Province, with high terrain and relatively scarce water resources [1]. In order to solve the water problems of local residents and promote the development of local economy, water diversion project was proposed and started to be implemented, the main target is to transfer water from other areas to central Yunnan to solve the local water problems, provide irrigation water source, and promote the development of local economy [2-3]. The water diversion project includes three main parts: water intake, water transmission and irrigation, in which the steel pipe welding process is an important process throughout the whole process [4].

Steel pipe welding construction process has a total of ten steps process: preparation, pipe mouth preheating, root welding, hot welding, filler welding, cover welding, post-weld insulation, surface cleaning, appearance inspection and repair, pipe section sealing [5]. The overall involves cleaning, measuring, cutting, trimming, assembling, selecting welding methods and materials, controlling welding parameters, welding technology, inspection methods, etc. Through correct operation and strict control, it can ensure the quality and continuity of pipeline welding and improve the strength and service life of welded joints [6-9]. Steel pipe welding construction is characterized by large mobility, small working surface, poor construction environment, many on-site operations, but also because of the complexity of the construction process has brought many problems.

First of all, the construction site with the construction progress and constantly migrate, compared with the factory production products, increased construction management, quality management, safety management and other aspects of the difficulty of welding operations in the flow state, to ensure the quality of the relative increase in the difficulty of a variety of terrain and ground attachments to the pipeline construction put forward higher requirements, but also prompted the pipeline welding construction should be adapted to the local conditions to choose different construction methods to meet the needs of the project, but also consider the wind, rain, snow, fog weather and temperature, humidity and other natural environment on the impact of welding quality [10-13]. Secondly, anticorrosive steel pipe and other joint weld welding operations with pipe welding, electric fire and other characteristics, there is a limited space operation asphyxiation, electrocution, fire, occupational disease (pneumoconiosis) and other safety risks [14-17]. Finally, steel pipe welding construction time is long, low efficiency is easy to affect the schedule; and because of the welding time is tight, in the encounter of other pipelines and obstacles need to lie down or turn construction, often in the localization of the dense weld, due to the quality can not be guaranteed and leakage often occurs, can not meet the requirements of the pipeline pressure test, non-destructive testing and acceptance of the completion of the project [18-20]. Therefore, it is necessary to optimize the welding process of steel pipe to improve the efficiency and ensure the construction quality at the same time.

In this paper, based on the displacement variational method, the simulation of the steel pipe welding process of the water diversion project in the middle of Yunnan Province is realized, and the process parameters of steel pipe welding are optimized. The simulation is mainly carried out from two aspects of temperature field and stress field, and the axial residual stress is simplified according to the simulation results. On the basis of the simulation, the radial basis function (RBF) neural network was used to fit the sample data, and then the particle swarm algorithm (PSO) was used to optimize the three main process parameters, namely, the opening angle, the current frequency, and the distance of the coil from the V-point, to find out the optimal values of the three main process parameters under the welding condition of the steel pipe of Dianzhong Diversion Project, so as to realize the optimized simulation of the welding process of the steel pipe.

2. Finite element simulation model of steel pipe welding process based on variational method

This paper realizes numerical simulation and optimal design of steel pipe welding process in Dianzhong water diversion project by constructing a finite element simulation model of steel pipe welding process and using the variational method to derive the radial displacement of steel pipe when it is subjected to the action of concentrated force.

2.1. Finite element simulation of steel pipe welding process

2.1.1. Welding Finite Element Simulation Technical Support:

1) Material ontology. The mechanical properties of a material are usually expressed using the stress-strain relationship, with the inclusion of a time variable in individual cases. Typically, materials are modeled by the principal structures of linear elasticity, elastoplasticity and viscoelasticity. The constitutive equation describing linear elasticity is:

$$\sigma = E\varepsilon \tag{1}$$

$$\tau = G\gamma \tag{2}$$

$$G = \frac{E}{2(1+\mu)} \tag{3}$$

Where: σ denotes stress. ε denotes strain. E denotes modulus of elasticity. G denotes shear modulus of elasticity. μ denotes Poisson's ratio.

When describing the elastic-plastic body, it should comply with the Mises yield criterion, often using multiple functions to cope with different problems, which can be divided into rigid-plastic model, ideal elastic-plastic model and linear reinforced elastic-plastic model.

(1) Rigid plasticity model:

$$\sigma = \sigma_s \tag{4}$$

(2) Ideal elastic-plastic model:

$$\begin{cases} \sigma = E\varepsilon, \varepsilon \le \varepsilon_s \\ \sigma = \sigma_s = E\varepsilon_s, \varepsilon \ge \varepsilon_s \end{cases} \tag{5}$$

(3) Linear reinforced elastoplastic model:

$$\begin{cases} \sigma = E\varepsilon, \varepsilon \le \varepsilon_s \\ \sigma = E\varepsilon_s + E\left(\varepsilon - \varepsilon_s\right), \varepsilon \ge \varepsilon_s \end{cases} \tag{6}$$

The viscoelastic model, on the other hand, studies creep and relaxation type of situations and is used in fewer scenarios in engineering analysis. Before selecting the material model, it is necessary to define the material properties, including the thermophysical parameters of the material, i.e., the modulus of elasticity, yield strength, specific heat and other parameters at different temperatures.

2) Heat source model. This is a mathematical expression relative to time and space summarized according to the distribution characteristics of heat input. According to different types of welding to choose a different heat source model, general arc welding using Gaussian heat source or double ellipsoid heat source model.

3) Life and death unit. The life and death unit perfectly reflects the region where the welding torch does not pass through, the weld is empty state, and the regional unit is activated when the welding torch passes through. In the case of a single pass weld, a set of cells should be defined during meshing,

and the set should be reactivated sequentially in the analysis step. And in the subsequent steps, the timing of the action of each heat dissipation surface should also be assigned according to the birth and death cells.

4) Heat engine coupling. It mainly contains two kinds of coupling, one is complete coupling and the other is sequential coupling. The difference is that the complete coupling is to solve the temperature field and stress field at the same time inside an incremental step, and the sequential coupling is to solve the completed sequential field first, and then solve the stress field later.

2.1.2. Basic flow of welding finite element simulation:

1) Welding simulation of the complete coupling method

The order of operation of the complete coupling is as follows:

Create a part → Define the material (thermophysical parameters at different temperatures) → Define the assembly → Define the analysis step (① Define the temperature-displacement coupling analysis step, ② Define the welding process and the cooling process) → Divide the mesh (encrypted mesh at the weld) → Define the interaction (boundary heat transfer) → Define the load (heat source model of the moving load) → Define the constraints (jigs and fixtures) → submit the Calculation (add heat source subroutine)

2) Welding simulation by the sequential coupling method. The sequence of operations for sequential coupling is as follows:

Create parts → Define materials (thermophysical parameters at different temperatures) → Define assembly → Define analysis steps (① Define temperature-displacement coupling analysis step, ② Define the welding process and the cooling process) → Divide the mesh (encrypted mesh at the weld) → Define interactions (boundary heat transfer) → Define load (heat source model of moving load) → Submit calculations (add heat source subroutine) → Change the analysis step (change to a generic analysis step with no change in the time of the analysis step) → Predefined field (import the temperature field from the previous result) → Define constraints (work fixture) → Solve the calculation.

2.1.3. Welding finite element method design. In this paper, Abaqus software is used for finite element analysis of steel pipe welding process [21]. In order to better understand the Abaqus simulation of the welding process, this time a single-layer single-pass welding and a multi-layer multi-pass welding were used for step-by-step advancement.

1) Single-layer single-pass welding. The single-layer single-pass welding model uses a steel pipe with an outer diameter of 159 mm and a wall thickness of 6 mm for finite element analysis. The welding bevel is determined in the simulation according to the welding process test of the gas guide tube and the actual welding situation. According to the ultrasonic flaw detection report, V-bevel along the circumference of the two sides of the test, did not see excessive defects, and V-bevel on the model requirements are low, more suitable for welding simulation. So this simulation of welding bevels using V-type bevels for finite element analysis.

Since Abaqus does not have a built-in unit system other than degrees, the International System of Units (SIU) was chosen as the unified unit standard for this simulation. When creating the part type, the features are selected as deformable tensile solids. In the Abaqus drawing process, follow the principle of first overall and then refinement, first draw the overall shape roughly, and then use to add dimensions to mark the lines, the long side of the input size of 20mm, of which 2mm is reserved for the weld seam. Select the short side to enter the new size of 4 mm, according to the 60 ° type bevel to determine the upper edge of the two points, automatic positioning to the midpoint of the drawing of the residual height of 1 mm, with three points to determine the arc of the arc of the upper edge of the weld to draw the arc, and ultimately get the required cross-section and weld size. The cross-section size and weld seam are shown in Figure 1.

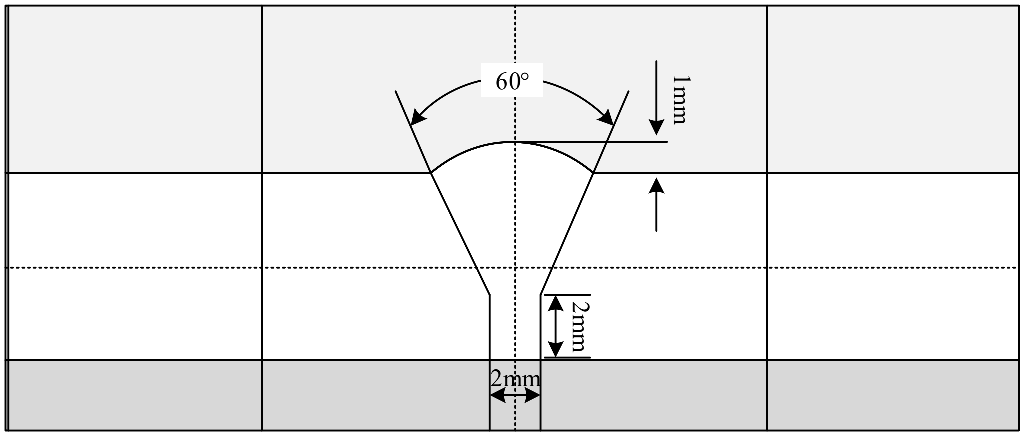

Fig. 1. Section size of single layer and single pass weld

In this paper, the weld and the base material are split and redefined by defining the cutting plane, and the meshes of the base material and the weld are defined at the same time. The base material is subjected to less thermal cycling and low residual stresses, so the mesh size decreases gradually from side to side, and when it reaches the weld, then the weld mesh is divided into a detailed and neat single one, which saves a lot of calculation time and improves the calculation accuracy.

For the single-layer single-pass welding simulation, the double ellipsoid heat source model is selected in this paper. The double ellipsoid heat source model is schematically shown in Figure 2. In the double ellipsoid heat source, with O as the origin, the first half, i.e., the smaller 1/4 ellipsoid, points to the forward direction of welding. There are four parameters that determine the shape in the double ellipsoid, i.e., different lengths of the two ellipsoids along the x-axis, the same width along the y-axis and the same depth along the z-axis. They are denoted as a_1, a_2, b, and c in the figure, respectively. b is related to the melt width and c is related to the melt depth in the heat source calibration process.

Formulae for the double ellipsoid heat source model (maximum heat flow density at the center):

The first half ellipsoid equation:

$$q_1(x,y,z)=\frac{6\sqrt{3}\left(f_1\phi\right)}{a_1 bc\pi\sqrt{\pi}}\exp\left(-3\left(\frac{x^2}{a_1^2}+\frac{y^2}{b^2}+\frac{z^2}{c^2}\right)\right),x\geq 0 \tag{7}$$

The posterior half ellipsoid formula:

$$q_2(x,y,z)=\frac{6\sqrt{3}\left(f_2\phi\right)}{a_2 bc\pi\sqrt{\pi}}\exp\left(-3\left(\frac{x^2}{a_2^2}+\frac{y^2}{b^2}+\frac{z^2}{c^2}\right)\right),x<0 \tag{8}$$

Where: a_1 indicates the length of the front half-axis in the welding direction. a_2 indicates the rear half-axis length in the welding direction. b indicates the half-axis length in the direction of weld width. c denotes the length of the half-axis in the direction of weld depth. f_1 and f_2 indicate the energy ratio of the front and back half ellipsoids, respectively. x indicates the distance from the center of the heat source in the direction of the weld. y indicates the distance from the center of the heat source in the direction of melt width. z denotes the distance from the center of heat source in the direction of melt depth.

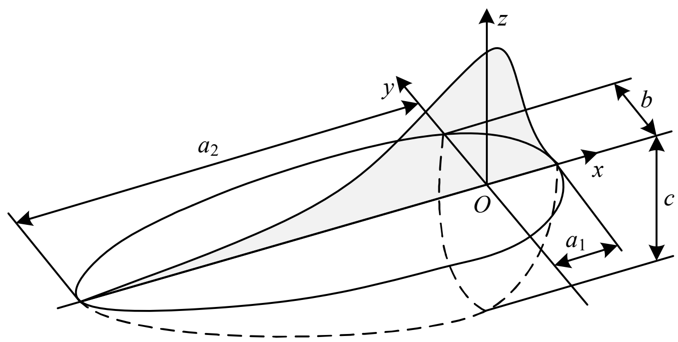

Fig. 2. Model of double ellipsoidal heat source

2) Multi-layer multi-pass welding. Compared with single-layer single-pass welding, multi-layer multi-pass welding is more complex, so the double ellipsoid heat source model is still chosen for the heat source model. Unlike single-layer single-pass welding, multi-layer multi-pass welding set up analysis step needs to establish a number of analysis steps, the first need to set up a very short time to kill the weld to the two steel pipe self-check, and then because of the design of the 7-layer 7-pass welding, each weld needs an analysis step, plus each weld needs to be set up after the welding of the cooling time of 12s, completely welded after the cooling time is set to 4800s, so the total of Multiple analysis steps are required, because the increase in analysis steps leads to a significant increase in simulation time. According to the welding speed input welding time, so that the welding simulation can be calculated smoothly, the welding time through the calculation is about 9724 s. In a whole welding process, the welding speed is the same, which if you want to change the welding speed of a particular weld, you can also be changed in the process of designing, so as to be able to use more flexible.

2.2. Derivation of radial displacement of steel pipe under force based on variational method

In order to better realize the optimized simulation of the welding process of steel pipe in Dianzhong Water Diversion Project, this paper chooses the displacement variational method (i.e., Ritz method) to derive the radial displacement of steel pipe when it is subjected to the action of concentrated force.

2.2.1. Variational methods. The variational method, mainly studies the generalized functions and their extremal solutions [22]. The so-called generalized function is a class of functions with a function as the independent variable, simply put, the generalized function is a function of a function. The generalized function studied in the variational method of elastodynamics is the energy of an elastic body, such as deformation potential energy, external potential energy, etc. Therefore, the variational method in elastodynamics is also known as the energy method.

It is assumed that the elastomer is always in equilibrium during the application of a force, so there is no change in kinetic energy, and there is no change in the non-mechanical energy of the elastomer, so the decrease in the potential energy of the external force is completely transformed into the deformation potential energy (also known as strain energy), which is stored in the interior of the elastomer. The deformation potential energy can be calculated as the work done by the stress on its corresponding strain.

In general, elastomers are not uniformly stressed, and the individual stress and deformation components are generally a function of positional coordinates, and thus the strain energy density v_ε is generally a function of positional coordinates. In order to be able to derive the deformation potential energy V_ε for the whole elastomer, the strain energy density v_ε must be integrated over the whole volume of the elastomer, i.e.:

$$V_\varepsilon = \frac{1}{2}\iiint\left(\sigma_x\varepsilon_x + \sigma_y\varepsilon_y + \sigma_z\varepsilon_z + \tau_{yz}\gamma_{yz} + \tau_z\gamma_{zx} + \tau_{xy}\gamma_{xy}\right)dxdydz \tag{9}$$

It can be seen that the deformation potential energy of an elastomer will not be negative regardless of its deformation. The deformation potential energy will be equal to zero only if all deformation components of the elastomer are equal to zero, which corresponds to a positive deformation potential energy under any deformation. The deformation potential energy is expressed in terms of the displacement components:

$$V_\varepsilon = \frac{E}{2(1+\mu)}\iiint\left[\frac{\mu}{1-2\mu}\left(\frac{\partial u}{\partial x}+\frac{\partial v}{\partial y}+\frac{\partial w}{\partial z}\right)^2+\left(\frac{\partial u}{\partial x}\right)^2+\left(\frac{\partial v}{\partial y}\right)^2+\left(\frac{\partial w}{\partial z}\right)^2 +\frac{1}{2}\left(\frac{\partial w}{\partial y}+\frac{\partial v}{\partial z}\right)^2+\frac{1}{2}\left(\frac{\partial u}{\partial z}+\frac{\partial w}{\partial x}\right)^2+\frac{1}{2}\left(\frac{\partial v}{\partial x}+\frac{\partial u}{\partial y}\right)^2\right]dxdydz \tag{10}$$

Suppose there is an arbitrary elastomer that is in equilibrium under the action of some external force. Lists u, v, and w are the displacement components actually present in this elastomer, and they satisfy the equilibrium differential equation expressed in terms of the displacement components, and satisfy the displacement boundary condition as well as the stress boundary condition expressed in terms of the displacement components. It is assumed that these displacement components undergo a small change allowed by the displacement boundary conditions, known as virtual displacement or displacement variance δu, δv, δw, becomes:

$$u' = u + \delta u, v' = v + \delta v, w' = w + \delta w \tag{11}$$

Assume that there is no change in velocity or temperature, and therefore no change in thermal or kinetic energy, of the elastomer during the virtual displacement. In this case, according to the theorem of conservation of energy, the increase in deformation potential energy should be equal to the decrease in the potential energy of the external force, which is also equal to the work done by the external force, i.e., the so-called virtual work. The external forces include the body forces with components f_x, f_y, and f_z, and the surface forces with components $\overline{f}_x$, $\overline{f}_y$, and $\overline{f}_z$, so the increase in deformation potential energy is seen to be:

$$\delta V_\varepsilon = \iiint\left(f_x dxdydz\delta u + f_y dxdydz\delta v + f_z dxdydz\delta w\right) + \iint\left(\overline{f}_x dS\delta u + \overline{f}_y dS\delta v + \overline{f}_z dS\delta w\right) \tag{12}$$

The triple integral in Eq. (12) must include the full volume of the elastomer. Since the virtual displacement or displacement variability δu, δv, and δw occurs as allowed by the displacement boundary conditions, $\delta u = \delta v = \delta w = 0$, on the constrained boundary, the triple integral of Eq. (12) need only include the full boundary area subject to the known surface forces. Equation (12) is obtained by collapsing it:

$$\delta V_\varepsilon = \iiint\left(f_x\delta u + f_y\delta v + f_z\delta w\right)dxdydz + \iint\left(\overline{f}_x\delta u + \overline{f}_y\delta v + \overline{f}_z\delta w\right)dS \tag{13}$$

Equation (13) is the so-called displacement variational equation, also known as the Lagrangian variational equation.

2.2.2. Ritz method. Ritz's method, one of the most important of the direct solutions of variational problems, is a computational method derived using the principle of minimum potential energy, the basic idea of which is not to consider the value of the generalized function in the tolerance function, but to approximate the extremal curves of the variational problem by a linear combination of a selected sequence of linearly uncorrelated functions [23]. An important role in structural analysis is to solve complex problems and their approximate solutions. Assume an expression for the displacement components such that the displacement boundary conditions are satisfied, but which contains several coefficients to be determined, and then determine these coefficients using the displacement variational equations.

Try to take the expression for the displacement component as follows:

$$u = u_0 + \sum_m A_m u_m, v = v_0 + \sum_m B_m v_m, w = w_0 + \sum_m C_m w_m \tag{14}$$

According to expression (13), the variational component of the displacement component is:

$$\delta u = \sum_m u_m \delta A_m, \delta v = \sum_m v_m \delta B_m, \delta w = \sum_m w_m \delta C_m \tag{15}$$

And the variation of the deformation potential energy is:

$$\delta V_\varepsilon = \sum_m \left(\frac{\partial V_\varepsilon}{\partial A_m} \delta A_m + \frac{\partial V_\varepsilon}{\partial B_m} \delta B_m + \frac{\partial V_\varepsilon}{\partial C_m} \delta C_m \right) \tag{16}$$

Bringing Eq. (15) and Eq. (16) into the displacement variational equation (13) gives:

$$\begin{aligned} &\sum_m \left(\frac{\partial V_\varepsilon}{\partial A_m} \delta A_m + \frac{\partial V_\varepsilon}{\partial B_m} \delta B_m + \frac{\partial V_\varepsilon}{\partial C_m} \delta C_m \right) \\ &= \sum_m \iiint \left(f_x u_m \delta A_m + f_y v_m \delta B_m + f_z w_m \delta C_m \right) dxdydz \\ &+ \iint \left(\overline{f}_x u_m \delta A_m + \overline{f}_y v_m \delta B_m + \overline{f}_z w_m \delta C_m \right) dS \end{aligned} \tag{17}$$

Perform a shifting term, which normalizes the variances of each coefficient to obtain:

$$\begin{aligned} &\sum_m \left[\frac{\partial V_\varepsilon}{\partial A_m} - \iiint f_x u_m dxdydz - \iint \overline{f}_x u_m dS \right] \delta A_m \\ &+ \sum_m \left[\frac{\partial V_\varepsilon}{\partial B_m} - \iiint f_y v_m dxdydz - \iint \overline{f}_y v_m dS \right] \delta B_m \\ &+ \sum_m \left[\frac{\partial V_\varepsilon}{\partial C_m} - \iiint f_z w_m dxdydz - \iint \overline{f}_z w_m dS \right] \delta C_m = 0 \end{aligned} \tag{18}$$

Since the variables δA_m, δB_m, and δC_m are completely arbitrary and independent of each other, their coefficients in the above equation must be equal to zero. Thus it is obtained:

$$\left. \begin{aligned} \frac{\partial V_\varepsilon}{\partial A_m} &= \iiint f_x u_m dxdydz + \iint \overline{f}_x u_m dS \\ \frac{\partial V_\varepsilon}{\partial B_m} &= \iiint f_y v_m dxdydz + \iint \overline{f}_y v_m dS \\ \frac{\partial V_\varepsilon}{\partial C_m} &= \iiint f_z w_m dxdydz + \iint \overline{f}_z w_m dS \\ &(m = 1, 2, 3, \cdots) \end{aligned} \right\} \tag{19}$$

Equation (19) is a primary equation for each coefficient. The equation can be solved for the individual coefficients and thus for the displacement components; this method is known as the Ritz method.

2.2.3. Derivation of steel pipe displacement using Ritz method. The steel pipe force model is shown in Fig. 3. The displacement component is set in the form of Eq. (10):

Radial displacement:

$$u = A_1 e^{-|z|} e^{\rho} + A_2 e^{-2|z|} e^{\rho} + A_3 e^{-3|z|} e^{\rho} + A_4 e^{-4|z|} e^{\rho} \tag{20}$$

This pipe can be regarded as an axisymmetric model, and its radial displacement is affected by both radial and axial directions due to the effect of annular concentrated force.

Circumferential displacement:

$$v = 0 \tag{21}$$

This pipe can be considered as an axisymmetric model, and annular displacement is not to be considered here.

Axial displacement:

$$w = C_1 e^{-|z|} + C_2 e^{-2|z|} + C_3 e^{-3|z|} + C_4 e^{-4|z|} \tag{22}$$

This pipe is an axisymmetric model, and its axial deformation is the same in all cross sections, independent of the radius.

Where: u , v, w is the displacement component, unit m. A, C is the 8 coefficients that do not depend on each other.

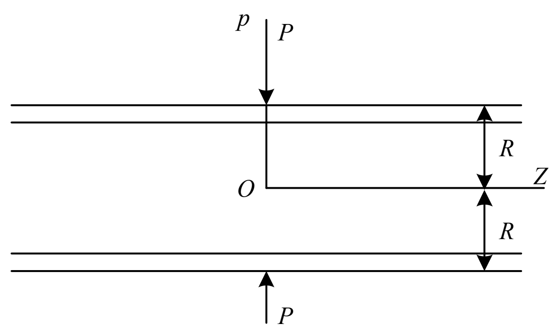

Fig. 3. Pipeline force model

Here, converting the right-angle coordinate system in which the equation is located to a column coordinate system, such that $x = \rho\cos\theta$, $y = \rho\sin\theta$, $z = z$, and $x^2 + y^2 = \rho^2$, we have:

$$\frac{\partial u}{\partial x} = \frac{\partial u}{\partial \rho}\frac{\partial \rho}{\partial x} + \frac{\partial u}{\partial \theta}\frac{\partial \theta}{\partial x}, \frac{\partial u}{\partial y} = \frac{\partial u}{\partial \rho}\frac{\partial \rho}{\partial y} + \frac{\partial u}{\partial \theta}\frac{\partial \theta}{\partial y} \tag{23}$$

Since this pipe can be considered as an axisymmetric model, the effect of its circumferential deformation is not considered here. Then:

$$\frac{\partial u}{\partial x} = \frac{\partial u}{\partial \rho}\frac{\partial \rho}{\partial x} = \left(A_1 e^{-|z|} + A_2 e^{-2|z|} + A_3 e^{-3|z|} + A_4 e^{-4|z|}\right) e^{\rho} \cos\theta \tag{24}$$

$$\frac{\partial u}{\partial y} = \frac{\partial u}{\partial \rho}\frac{\partial \rho}{\partial y} = \left(A_1 e^{-|z|} + A_2 e^{-2|z|} + A_3 e^{-3|z|} + A_4 e^{-4|z|}\right) e^{\rho} \sin\theta \tag{25}$$

Then it is known that the deformation potential energy of the pipe i.e. Eq. (10) is expressed in terms of the displacement component:

$$V_{\xi} = \frac{E}{2(1+\mu)} \iiint \left[\frac{\mu}{1-2\mu} \left(\frac{\partial u}{\partial \rho}\frac{\partial \rho}{\partial x} + \frac{\partial w}{\partial z} \right)^2 + \left(\frac{\partial u}{\partial \rho}\frac{\partial \rho}{\partial x} \right)^2 + \left(\frac{\partial w}{\partial z} \right)^2 + \frac{1}{2}\left(\frac{\partial u}{\partial z} \right)^2 + \frac{1}{2}\left(\frac{\partial u}{\partial \rho}\frac{\partial \rho}{\partial y} \right)^2 \right] \rho d\rho d\theta dz \tag{26}$$

Where: E is the modulus of elasticity in GP. μ is the Poisson's ratio. u and w are displacement components.

When $z>0$ is present:

$$\begin{aligned}
V_{\xi(z>0)} &= \frac{E}{2(1+\mu)}\iiint\left\{\frac{\mu}{1-2\mu}\left[\left(A_1e^{-z}+A_2e^{-2z}+A_3e^{-3z}+A_4e^{-4z}\right)e^{\rho}\right.\right.\\
&\left.\cos\theta - C_1e^{-z}-2C_2e^{-2z}-3C_3e^{-3z}-4C_4e^{-4z}\right]^2\rho d\rho d\theta dz\\
&+\left[\left(A_1e^{-z}+A_2e^{-2z}+A_3e^{-3z}+A_4e^{-4z}\right)e^{\rho}\cos\theta\right]^2\rho d\rho d\theta dz\\
&+\left(-C_1e^{-z}-2C_2e^{-2z}-3C_3e^{-3z}-4C_4e^{-4z}\right)^2\rho d\rho d\theta dz\\
&+\frac{1}{2}\left[\left(-A_1e^{-z}-2A_2e^{-2z}-3A_3e^{-3z}-4A_4e^{-4z}\right)e^{\rho}\right]^2\rho d\\
&\left.\frac{1}{2}\left[\left(A_1e^{-z}+A_2e^{-2z}+A_3e^{-3z}+A_4e^{-4z}\right)e^{\rho}\sin\theta\right]^2\rho d\rho d\theta dz\right\}\\
&=\frac{E}{2(1+\mu)}\left[\iiint\frac{1-\mu}{1-2\mu}\left[\left(A_1e^{-z}+A_2e^{-2z}+A_3e^{-3z}+A_4e^{-4z}\right)^2e^{2\rho}\cos^2\theta\right.\right.\\
&\rho d\rho d\theta dz+\frac{1-\mu}{1-2\mu}\left(-C_1e^{-z}-2C_2e^{-2z}-3C_3e^{-3z}-4C_4e^{-4z}\right)^2\rho d\rho d\theta dz\\
&+\frac{\mu}{1-2\mu}\left(A_1e^{-z}+A_2e^{-2z}+A_3e^{-3z}+A_4e^{-4z}\right)\\
&\left(-C_1e^{-z}-2C_2e^{-2z}-3C_3e^{-3z}-4C_4e^{-4z}\right)e^{\rho}\cos\theta\rho d\rho d\theta dz\\
&+\frac{1}{2}\left(-A_1e^{-z}-2A_2e^{-2z}-3A_3e^{-3z}-4A_4e^{-4z}\right)^2e^{2\rho}\rho d\rho d\theta dz\\
&\left.+\frac{1}{2}\left(A_1e^{-z}+A_2e^{-2z}+A_3e^{-3z}+A_4e^{-4z}\right)^2e^{2\rho}\sin^2\theta\rho d\rho d\theta dz\right\}\\
&=\frac{E}{2(1+\mu)}\left\{\frac{3-4\mu}{4(1-2\mu)}[(Re^{2R}-re^{2r})-\frac{1}{2}(e^{2R}-e^{2r})]\pi\right.\\
&\left(\frac{1}{2}A_1^2+\frac{1}{4}A_2^2+\frac{1}{6}A_3^2+\frac{1}{8}A_4^2+\frac{2}{3}A_1A_2+\frac{1}{2}A_1A_3+\frac{2}{5}A_1A_4\right.\\
&\left.+\frac{2}{5}A_2A_3+\frac{1}{3}A_2A_4+\frac{2}{7}A_3A_4\right)+\frac{1}{2}\left[\left(\mathrm{Re}^{2R}-re^{2r}\right)-\frac{1}{2}\left(e^{2R}-e^{2r}\right)\right]\\
&\pi\left(\frac{1}{2}A_1^2+A_2^2+\frac{3}{2}A_3^2+2A_4^2+\frac{4}{3}A_1A_2+\frac{3}{2}A_1A_3+\frac{8}{5}A_1A_4+\frac{12}{5}A_2A_3\right.\\
&\left.+\frac{8}{3}A_2A_4+\frac{24}{7}A_3A_4\right)+\frac{1-\mu}{1-2\mu}\left(R^2-r^2\right)\pi\left(\frac{1}{2}C_1^2+C_2^2+\frac{3}{2}C_3^2\right.\\
&\left.\left.+2C_4^2+\frac{4}{3}C_1C_2+\frac{3}{2}C_1C_3+\frac{8}{5}C_1C_4+\frac{12}{5}C_2C_3+\frac{8}{3}C_2C_4+\frac{24}{7}C_3C_4\right)\right\}
\end{aligned} \tag{27}$$

$V_{\xi(z<0)}=V_{\xi(z>0)}$ when $z<0$.

It follows that the total deformation potential energy is:

$$\begin{aligned}V_{\xi}=\frac{E}{1+\mu}\Bigg\{&\frac{3-4\mu}{4(1-2\mu)}[(Re^{2R}-re^{2r})-\frac{1}{2}(e^{2R}-e^{2r})]\\&\pi\left(\frac{1}{2}A_1^2+\frac{1}{4}A_2^2+\frac{1}{6}A_3^2+\frac{1}{8}A_4^2+\frac{2}{3}A_1A_2+\frac{1}{2}A_1A_3\right.\\&\left.+\frac{2}{5}A_1A_4+\frac{2}{5}A_2A_3+\frac{1}{3}A_2A_4+\frac{2}{7}A_3A_4\right)\\&+\frac{1}{2}\left[\left(\mathrm{Re}^{2R}-re^{2r}\right)-\frac{1}{2}\left(e^{2R}-e^{2r}\right)\right]\\&\pi\left(\frac{1}{2}A_1^2+A_2^2+\frac{3}{2}A_3^2+2A_4^2+\frac{4}{3}A_1A_2+\frac{3}{2}A_1A_3\right.\\&\left.+\frac{8}{5}A_1A_4+\frac{12}{5}A_2A_3+\frac{8}{3}A_2A_4+\frac{24}{7}A_3A_4\right)\\&+\frac{1-\mu}{1-2\mu}\left(R^2-r^2\right)\pi\left(\frac{1}{2}C_1^2+C_2^2+\frac{3}{2}C_3^2\right.\\&\left.+2C_4^2+\frac{4}{3}C_1C_2+\frac{3}{2}C_1C_3+\frac{8}{5}C_1C_4+\frac{12}{5}C_2C_3+\frac{8}{3}C_2C_4+\frac{24}{7}C_3C_4\right)\Bigg\}\end{aligned} \tag{28}$$

Derive here for V_{ξ}:

$$\begin{aligned}\frac{\partial V_{\xi}}{\partial A_1}=\frac{E}{1+\mu}\Bigg\{&\frac{3-4\mu}{4(1-2\mu)}\left[\left(\mathrm{Re}^{2R}-re^{2r}\right)-\frac{1}{2}\left(e^{2R}-e^{2r}\right)\right]\\&\pi\left(A_1+\frac{2}{3}A_2+\frac{1}{2}A_3+\frac{2}{5}A_4\right)\\&+\frac{1}{2}\left[\left(\mathrm{Re}^{2R}-re^{2r}\right)-\frac{1}{2}\left(e^{2R}-e^{2r}\right)\right]\pi\left(A_1+\frac{4}{3}A_2+\frac{3}{2}A_3+\frac{8}{5}A_4\right)\Bigg\}\end{aligned} \tag{29}$$

$$\begin{aligned}\frac{\partial V_{\xi}}{\partial A_2}=\frac{E}{1+\mu}\Bigg\{&\frac{3-4\mu}{4(1-2\mu)}\left[\left(\mathrm{Re}^{2R}-re^{2r}\right)-\frac{1}{2}\left(e^{2R}-e^{2r}\right)\right]\\&\pi\left(\frac{2}{3}A_1+\frac{1}{2}A_2+\frac{2}{5}A_3+\frac{1}{3}A_4\right)\\&+\frac{1}{2}\left[\left(\mathrm{Re}^{2R}-re^{2r}\right)-\frac{1}{2}\left(e^{2R}-e^{2r}\right)\right]\pi\left(\frac{4}{3}A_1+2A_2+\frac{12}{5}A_3+\frac{8}{3}A_4\right)\Bigg\}\end{aligned} \tag{30}$$

$$\begin{aligned}\frac{\partial V_{\xi}}{\partial A_3}=\frac{E}{1+\mu}\Bigg\{&\frac{3-4\mu}{4(1-2\mu)}\left[\left(\mathrm{Re}^{2R}-re^{2r}\right)-\frac{1}{2}\left(e^{2R}-e^{2r}\right)\right]\\&\pi\left(\frac{1}{2}A_1+\frac{2}{5}A_2+\frac{1}{3}A_3+\frac{2}{7}A_4\right)+\frac{1}{2}\left[\left(\mathrm{Re}^{2R}-re^{2r}\right)-\frac{1}{2}\left(e^{2R}-e^{2r}\right)\right]\\&\pi\left(\frac{3}{2}A_1+\frac{12}{5}A_2+3A_3+\frac{24}{7}A_4\right)\Bigg\}\end{aligned} \tag{31}$$

$$\begin{aligned}\frac{\partial V_{\xi}}{\partial A_4}=\frac{E}{1+\mu}\left\{\frac{3-4\mu}{4(1-2\mu)}\left[\left(\mathrm{Re}^{2R}-re^{2r}\right)-\frac{1}{2}\left(e^{2R}-e^{2r}\right)\right]\right.\\ \pi\left(\frac{2}{5}A_1+\frac{1}{3}A_2+\frac{2}{7}A_3+\frac{1}{4}A_4\right)+\frac{1}{2}\left[\left(\mathrm{Re}^{2R}-re^{2r}\right)-\frac{1}{2}\left(e^{2R}-e^{2r}\right)\right]\\ \left.\pi\left(\frac{8}{5}A_1+\frac{8}{3}A_2+\frac{24}{7}A_3+4A_4\right)\right\}\end{aligned} \tag{32}$$

Applying the Ritz method of displacement variational method, take $\mu_1=e^{-|z|}e^R$, $\mu_2=e^{-2|z|}e^R$, $\mu_3=e^{-3|z|}e^R$, $\mu_4=e^{-4|z|}e^R$, μ_1, μ_2, μ_3, μ_4 directions are radial.

According to the thick-walled cylinder force can be known body force is zero, radial surface force $\overline{f_\rho}=-P$. Then there:

$$\left.\begin{aligned}&\frac{\partial V_{\xi}}{\partial A_1}=\iiint f_x\mu_1 dxdydz+\iint \overline{x}_x\mu_1 dS=\iint \overline{f_\rho}\mu_1 dS=-2\pi Pe^R R\\ &\frac{\partial V_{\xi}}{\partial A_2}=-2\pi Pe^R R\\ &\frac{\partial V_{\xi}}{\partial A_3}=-2\pi Pe^R R\\ &\frac{\partial V_{\xi}}{\partial A_4}=-2\pi Pe^R R\end{aligned}\right\} \tag{33}$$

Bringing Eqs. (20) to (22) and Eq. (26) into Eq. (33) shows the following equation:

$$\left.\begin{aligned}&\frac{E}{1+\mu}\left\{\frac{3-4\mu}{4(1-2\mu)}M\left(A_1+\frac{2}{3}A_2+\frac{1}{2}A_3+\frac{2}{5}A_4\right)\right.\\ &\left.+\frac{1}{2}M\left(A_1+\frac{4}{3}A_2+\frac{3}{2}A_3+\frac{8}{5}A_4\right)\right\}=-2\pi Pe^R R\\ &\frac{E}{1+\mu}\left\{\frac{3-4\mu}{4(1-2\mu)}M\left(\frac{2}{3}A_1+\frac{1}{2}A_2+\frac{2}{5}A_3+\frac{1}{3}A_4\right)\right.\\ &\left.+\frac{1}{2}M\left(\frac{4}{3}A_1+2A_2+\frac{12}{5}A_3+\frac{8}{3}A_4\right)\right\}=-2\pi Pe^R R\\ &\frac{E}{1+\mu}\left\{\frac{3-4\mu}{4(1-2\mu)}M\left(\frac{1}{2}A_1+\frac{2}{5}A_2+\frac{1}{3}A_3+\frac{2}{7}A_4\right)\right.\\ &\left.+\frac{1}{2}M\left(\frac{3}{2}A_1+\frac{12}{5}A_2+3A_3+\frac{24}{7}A_4\right)\right\}=-2\pi Pe^R R\\ &\frac{E}{1+\mu}\left\{\frac{3-4\mu}{4(1-2\mu)}M\left(\frac{2}{5}A_1+\frac{1}{3}A_2+\frac{2}{7}A_3+\frac{1}{4}A_4\right)\right.\\ &\left.+\frac{1}{2}M\left(\frac{8}{5}A_1+\frac{8}{3}A_2+\frac{24}{7}A_3+4A_4\right)\right\}=-2\pi Pe^R R\end{aligned}\right\} \tag{34}$$

To simplify the calculation, it is taken in the operation:

$$M=\left[\left(\mathrm{Re}^{2R}-re^{2r}\right)-\frac{1}{2}\left(e^{2R}-e^{2r}\right)\right]\pi \tag{35}$$

Solve for M by bringing it into Equation (f):

$$A_1 = K_1 NP, A_2 = K_2 NP$$
$$A_3 = K_3 NP, A_4 = K_4 NP \tag{36}$$

To further simplify the calculation process take in the above equation:

$$K_1 = \frac{40(4\mu-9)(\mu-4)(\mu+299)}{-16\mu^4+8920\mu^3+278527\mu^2+475355\mu+43164} \tag{37}$$

$$K_2 = -\frac{90(4\mu-1)(4\mu-9)(\mu-4)}{-16\mu^4+8920\mu^3+278527\mu^2+475355\mu+43164} \tag{38}$$

$$K_3 = \frac{840(4\mu-1)(\mu-4)(\mu-151)}{-16\mu^4+8920\mu^3+278527\mu^2+475355\mu+43164} \tag{39}$$

$$K_4 = -\frac{140(4\mu-1)(4\mu-9)(\mu-241)}{-16\mu^4+8920\mu^3+278527\mu^2+475355\mu+43164} \tag{40}$$

$$N = \frac{-2e^R R(1+\mu)\pi}{EM} \tag{41}$$

Therefore, the radial displacement at each place of the pipe can be solved as:

$$u_4 = \left(K_l e^{-|z|} + K_2 e^{-2|z|} + K_3 e^{-3|z|} + K_4 e^{-4|z|}\right) N e^{\rho} P \tag{42}$$

2.3. Simulation results and analysis

2.3.1. Analysis of temperature field simulation results. Welding process, due to the extreme inhomogeneity of the heat input, and the heat source is also in a state of constant movement, so the temperature field in the weldment changes sharply with time and space, and there is a large temperature gradient in the weldment, the accuracy of the results of the temperature field calculation of the weldment in each region depends on the simulation process to establish the geometric model, the material model, the boundary conditions, and so on, and the results of the temperature field calculations will be The temperature field calculation results will directly affect the accuracy of the subsequent welding stress field calculation results. The melting point of the selected Q420 steel is about 1450 ℃, the simulation will be more than 1450 ℃ part of the definition of the weld pool, according to the built three-dimensional model, using the corresponding mesh division, heat source parameters, process parameters, boundary conditions, the calculation of the Q420 large-diameter thick-walled steel pipe welding transient temperature field results.

The temperature time course curve extraction node is shown in Figure 4. Seven nodes named W1-W7 are extracted at equal spacing along the circumference of the weld on the surface of the weld, seven nodes named D1-D7 are extracted along the circumference of the weld in the heat-affected zone, seven nodes named LI-L7 are extracted along the circumference of the weld in parallel with the W1-W7, seven nodes named LI-L7 are extracted along the base material away from the weld in parallel with the WI-W7, then one node is extracted in the inner wall of the pipe in the direction perpendicular to the weld at intervals of 10mm in the weld and the heat-affected zone, and a node corresponding to the position of 20mm is extracted at intervals far away from the weld. Then in the direction of vertical weld in the inner wall of the steel pipe, a node is taken at an interval of 10mm in the weld and heat affected zone, and a node is taken at an interval of 20mm away from the weld, and a total of 10 nodes are taken in the direction of vertical weld, and the corresponding positions in the inner wall of the steel pipe are taken at the points HI-H10 in Figure 4. Finally, the temperature time profile of these nodes is extracted.

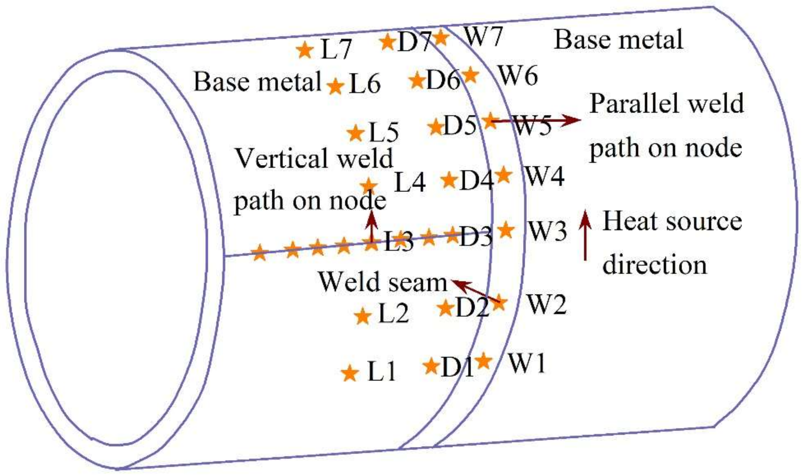

Fig. 4. Nodes for extracting temperature time history curves

The equidistant node temperature time profile taken in the weld zone is shown in Figure 5. From Fig. 5, it can be seen that in the welding heating process, when the heat source moves to a certain point, the temperature of this point rises rapidly until the maximum value, and then drops rapidly as the heat source leaves, and the temperature drops rapidly to 300 ℃, and then the cooling rate slows down until the room temperature state. Because the nodes W1-W7 in the model symmetry surface, in the last weld surface, in the welding of other welds this weld belongs to the inactive state, the node temperature is always in the room temperature, when welding to the node position, the unit is activated by the welding heat source heated by the node temperature rises rapidly to reach the maximum temperature. So there is only one wave peak in each curve, and by comparing the rising and falling stages of the curve, it can be seen that the rate of temperature rise is obviously greater than the rate of fall, and after entering the quasi-steady state, the temperature change process at each point is the same.

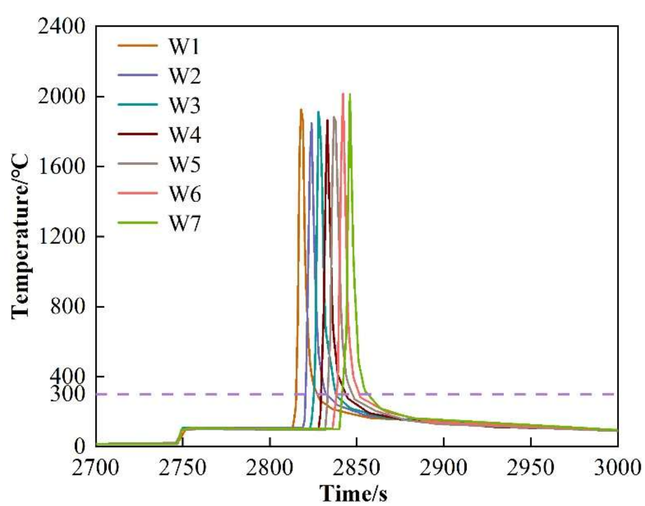

Fig. 5. W1-W7 temperature history curve

The temperature time-course curves of nodes D1-D7 are shown in Fig. 6, and the D1 curve is shown in Fig. 7. Because these seven points are located on the base material and do not undergo the process of unit life and death, it can be seen from the D1 curve that each curve has a total of 17 wave peaks, which side by side confirms that the member has undergone 17 welding heating process. And each wave peak has high and low, this is because of the influence of the welding order of the weld channel, this study uses the symmetric welding process, the welding order of the weld channel is symmetric about the member symmetric section symmetric, in the symmetric part of the weld is the last weld channel welded in each layer of the weld. The temperature is high when the weld passes are close to the nodes taken and the temperature peak is lower when the weld passes are farther away from the nodes.

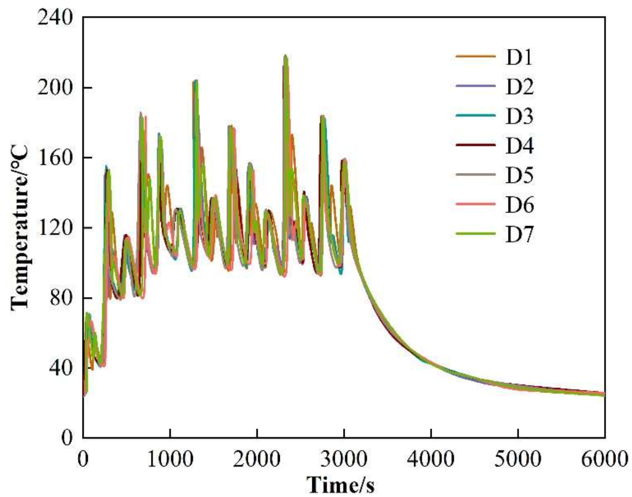

Fig. 6. D1-D7 Temperature history curve

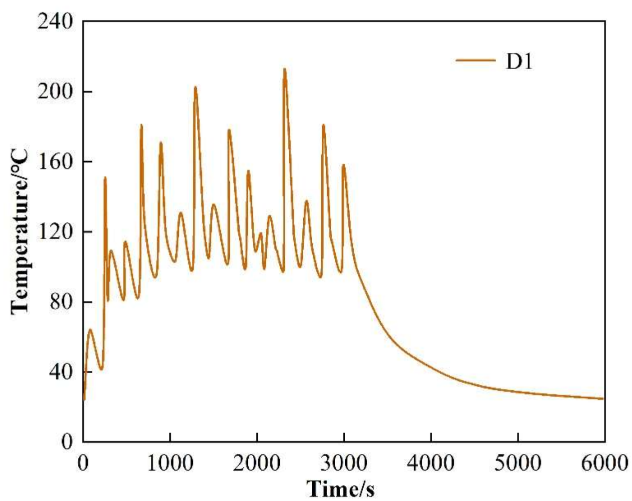

Fig. 7. Temperature history curve on D1

The temperature time-course curves of nodes L1-L7 are shown in Fig. 8, and the D1 curves are shown in Fig. 9. Since nodes L1-L7 are also located on the base material and do not undergo the process of unit life and death, there are 17 peaks in each temperature time course curve, but compared with the temperature time course curves of nodes D1-D7, the overall temperature of L1-L7 is lower, which is due to the fact that L1-L7 is further away from the weld compared to D1-D7 and the difference in the peaks between the different peaks is smaller, which is due to the fact that the distance from the weld is farther and the difference in the distance from different weld to the node is This is due to the fact that the distance from the seam is farther and the difference between the peaks of different welds from the node is smaller.

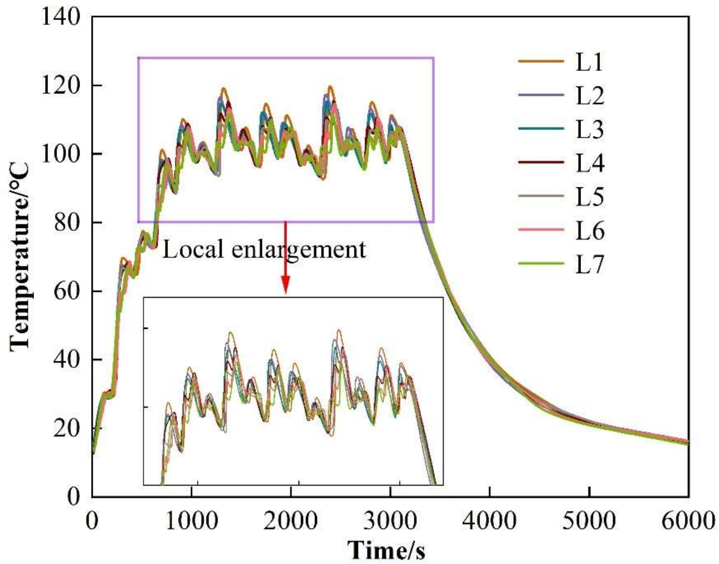

Fig. 8. L1-L7 Temperature history curve

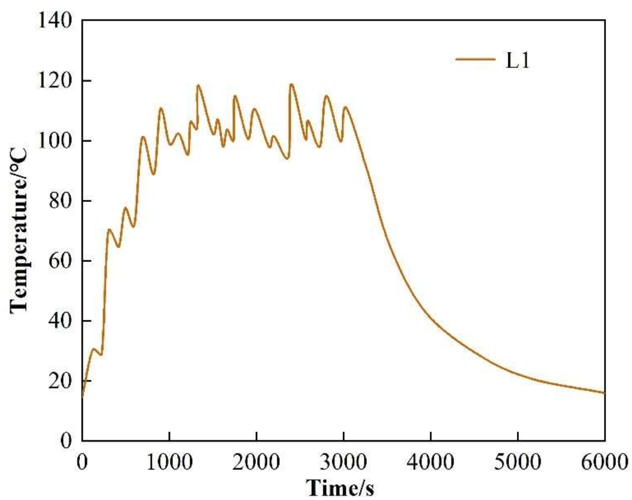

Fig. 9. Temperature history curve on L1

The time course profile of the temperature at the equidistant node taken along the direction of the vertical weld path is shown in Fig. 10. When the welding heat source moves to the cross-section, the cross-section temperature rises sharply, and the peak temperature in the weld region reaches more than 2100℃. After the heat source moved through the rapid decline in temperature, and the same rule of temperature change on the weld center line, the rate of temperature rise is obviously faster than the decline, and due to heat conduction, the peak temperature of each point with the distance from the center of the weld increases and decreases, combined with the local zoom in Figure 10 can be seen that the time to reach the peak temperature is also lagging behind.

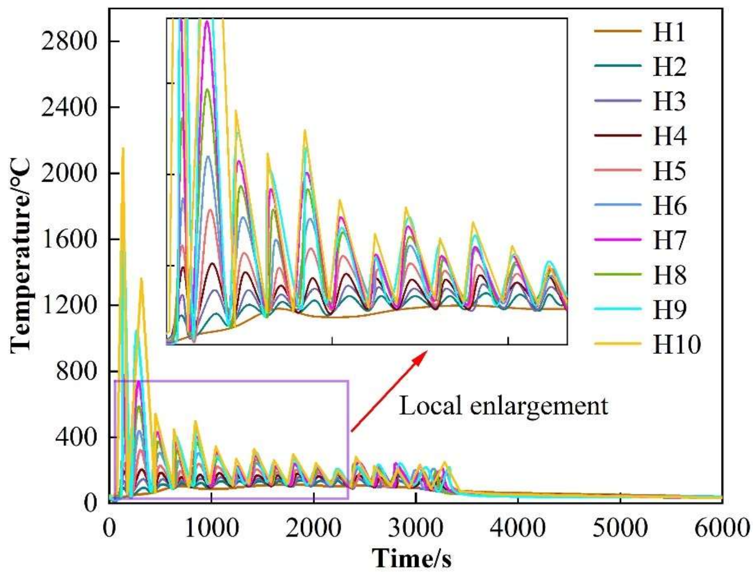

Fig. 10. H1-H10 Temperature history curve

The temperature time curve extracted from each point of 1-17 weld passes on a certain section is shown in Fig. 11, from which it can be seen that the peak temperature at the node of each weld is similar, and is around 2100℃.

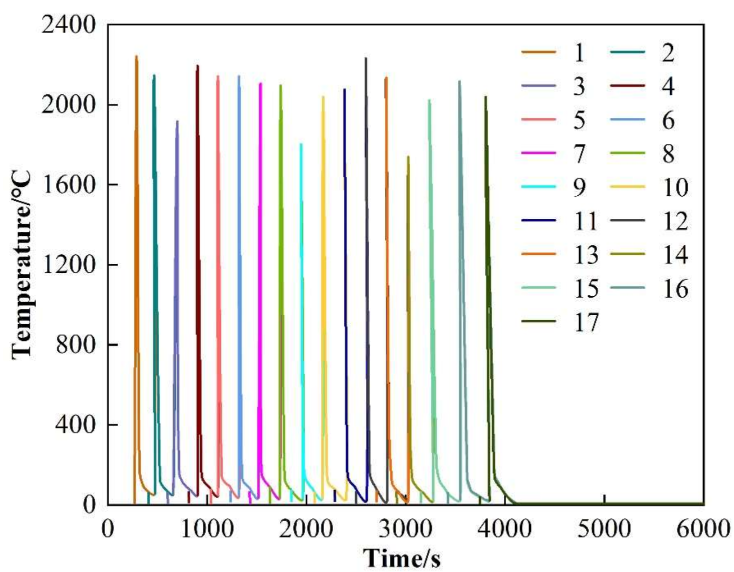

Fig. 11. Temperature time history curve of each solder path node in the same section

The 1st weld node, the 10th weld node, the 15th weld node, and the 17th weld node temperature time course profiles are shown in Fig. 12, Fig. 13, Fig. 14, and Fig. 15, respectively. Figure 12 has 17 peaks because the first weld is the earliest activated weld, Figure 13 has 8 peaks because weld 10 was not activated when the first 9 welds were welded, the first weld and the 8th peak are higher than the other 6 peaks in the figure because of the position of the 10th weld and the 17th weld, and the 17th weld is right next to the 10th weld, so the 17th weld is not activated when welding the 10th weld, and the 10th weld is not activated when welding the 17th weld. The 17th weld is directly above the 10th weld, so the welding of the 17th weld has a greater effect on the temperature of the node on the 10th weld. The 5th to 7th peaks are higher than the 2nd to 4th peaks, also because the 14th to 16th weld passes are closer to the 10th pass than the 11th to 13th passes. As can be seen from Fig. 14, the temperature time profile has 3 peaks. As can be seen from Fig. 15, there is only 1 wave peak because the 17th weld node is the last activated weld. From the above analysis, it can be seen that the results of this welding temperature field simulation are very reasonable and can accurately describe the change process of the welding temperature field of the large-diameter thick-walled steel pipe under this welding process. This is one of the keys to obtain an accurate welding residual stress field.

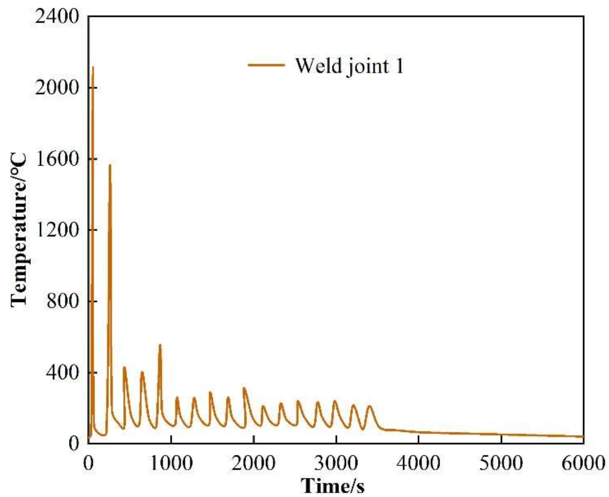

Fig. 12. Temperature history curve of the first weld joint

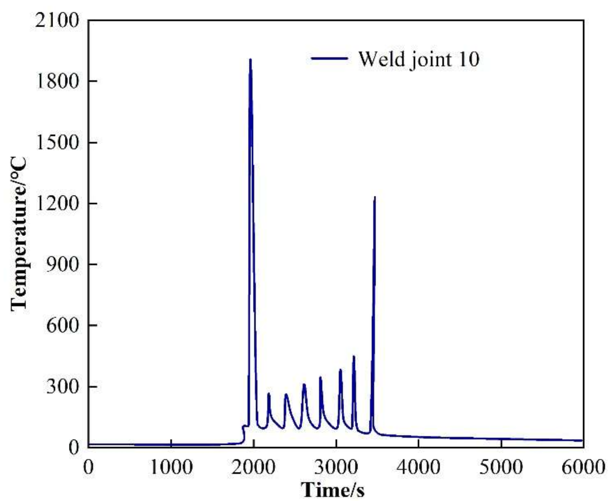

Fig. 13. Temperature history curve of the tenth weld joint

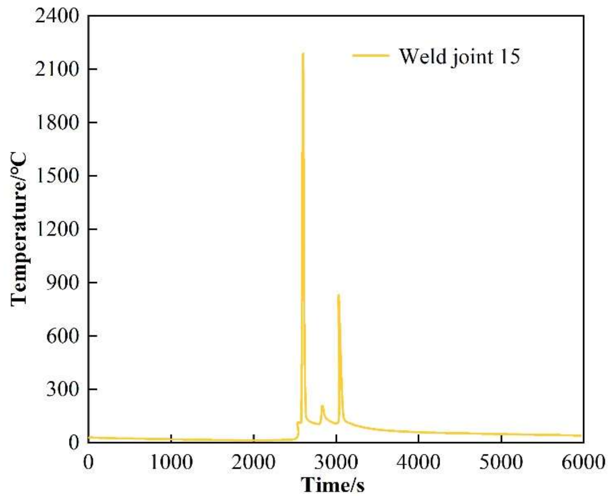

Fig. 14. Temperature history curve of the fifteenth weld joint

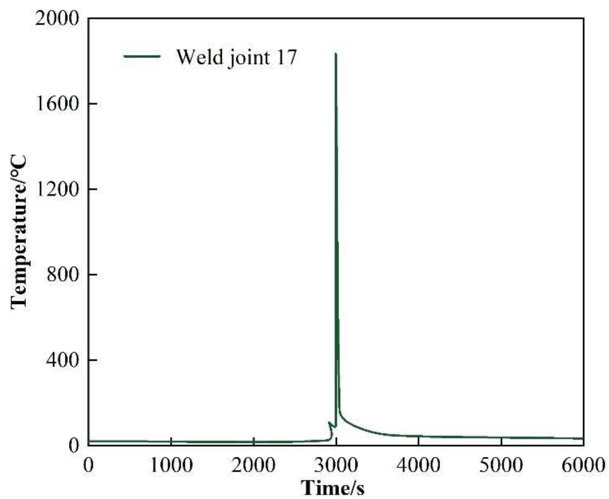

Fig. 15. Temperature history curve of the seventeenth weld joint

2.3.2. Analysis of stress field simulation results. Based on the welding temperature field to further solve the welding stress field, components in the actual welding process requires fixtures to be fixed, in the welding simulation process in order to match the actual situation, the displacement constraints loaded in the course of this study: welding process in the symmetry plane node symmetry constraints, symmetry constraints is the principle of constraints on the symmetry plane nodes perpendicular symmetry plane direction of the displacement of nodes along the symmetry plane nodes can be rotated along the symmetry plane, translational, and so on. Nodes on the symmetry plane can rotate and translate along the symmetry plane. At the same time on both ends of the steel pipe member cross-section nodes for fixed constraints, in the cooling stage: the same symmetry constraints in the symmetry plane, while releasing the fixed constraints on the nodes of the two ends of the steel pipe cross-section, and only at one end of the cross-section of the three nodes selected for the minimum constraints to prevent displacement of the rigid body, so that the component can be free to deform. In the welding stress field calculation process the material adopts isotropic isotropic strengthening model, and the material obeys the Von mise yield criterion. And the effect of strain hardening of the material on the welding residual stress field of the steel pipe is considered.

In order to obtain the distribution pattern of the residual stress along the axial direction of the thick-walled steel pipe, two paths need to be defined on the inner and outer surfaces of the steel pipe along the axial direction, and the residual stress values at the nodes are extracted along the paths, and then plotted as stress curves. The defined extracted stress paths are shown in Fig. 16, and the nodes on the paths are the nodes obtained by model meshing.

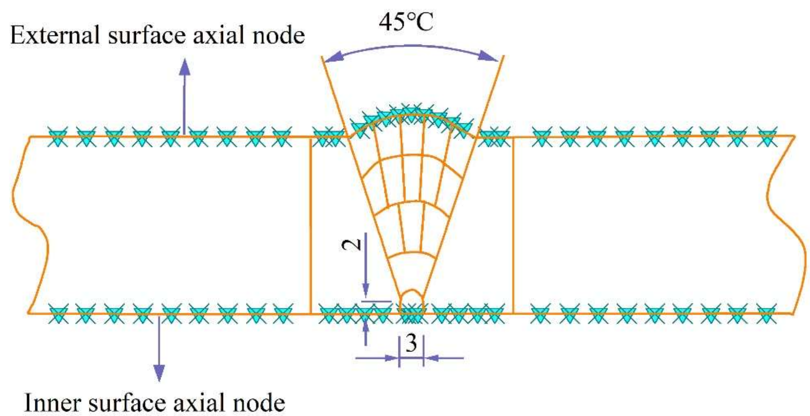

Fig. 16. Stress extraction path

The residual stress curve on the inner surface of the steel pipe is shown in Fig. 17, and the residual stress curve on the outer surface of the steel pipe is shown in Fig. 18. The horizontal coordinate of the stress curve is the distance from the node to the origin, and the vertical coordinate is the value of the residual stress on the node.

Combined with Figure 17 and Figure 18, it can be seen that there is a great difference in the stress on the path of the inner and outer walls of the steel pipe, the equivalent residual stresses on the inner and outer walls of the steel pipe are similar, and the maximum value has reached the yield strength of the material. While the annular residual stress and axial residual stress in the inner and outer walls of the pipe are more different, the annular residual stress in the weld and heat-affected zone is compressive stress, the maximum value of which reaches the nominal yield strength of the material, while the annular residual stress in the inner wall of the pipe is tensile stress in the weld and heat-affected zone, and the maximum value of which also reaches the yield strength of the material. Axial residual stress in the pipe wall weld and heat-affected zone for compressive stress, compressive stress maximum value of 0.7 times the material yield strength, while the pipe wall weld and heat-affected zone axial residual stress for tensile stress, tensile stress maximum value of 0.4 times the material yield strength.

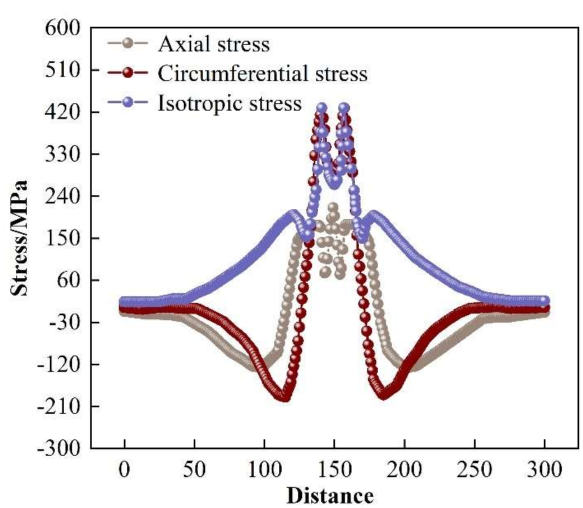

Fig. 17. Residual stress curve of the inner surface of the steel pipe

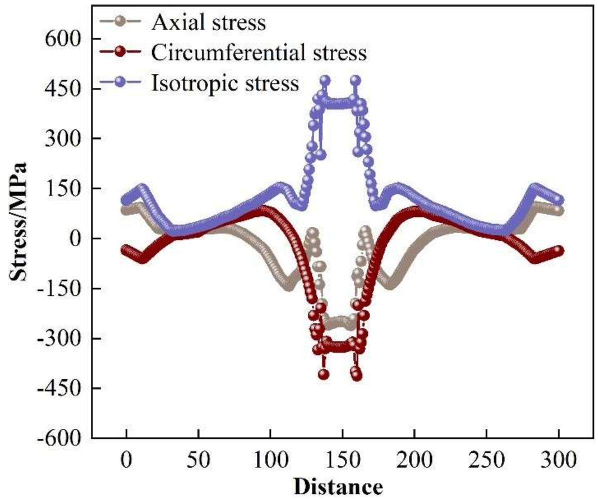

Fig. 18. Residual stress curve of the outer surface of the steel pipe

2.3.3. Simplified illustration of axial residual stresses. Through the calculation and analysis, it can be seen that the axial residual stress in the inner and outer walls of the steel pipe along the axial distribution in the form of a curve, in order to calculate the stable bearing capacity of welded steel pipe to facilitate the input of residual stress, this paper refers to the results of the finite element calculation of the distribution of residual stress curve, the use of straight instead of curved method will be the steel pipe butt weld axial residual stress distribution for a reasonable simplification. The simplification process follows the principle of internal force equivalence and self-equilibrium of internal forces, by adjusting the area enclosed by the tensile and compressive stress straight line and x-axis in the simplified illustration with the same curve as the original curve, the tensile stress area of the inner wall of the pipe is simplified as a trapezium, and the compressive stress area is simplified as a triangle, while the outer wall of the pipe is just the opposite, the compressive stress area is simplified as a trapezium, and the tensile stress area is simplified as a triangle. Simplified in the direction of the wall thickness of the pipe stress is a linear change, and in the entire cross-section of the tensile and compressive stress is balanced. Engineering more commonly used thick-walled steel pipe diameter thickness ratio in the vicinity of 18, so this paper for the diameter thickness ratio of 18 butt-welded steel pipe axial weld residual stresses proposed by the corresponding simplified distribution model.

The axial residual stress is simplified as shown in Figure 19, Figure (a) ~ (b), respectively, represents the simplified residual stress in the inner wall of the pipe and the simplified residual stress in the outer wall of the pipe, of which W is the width of the weld, Fy for the material yield strength. As can be seen from Fig. 19, in the weld part of the inner wall of the pipe is 0.4 times the yield strength of the material tensile stress, in the heat-affected zone is 0.2 times the yield strength of the material compressive stress, away from the weld part of the stress is 0, during the period of the stress is a linear excess. In the weld part of the outer wall of the pipe it is 0.7 times the yield strength of the material and in the heat affected zone it is 0.3 times the tensile residual stress. The value of stress in the area away from the weld is 0, during which the linear excess is carried out.

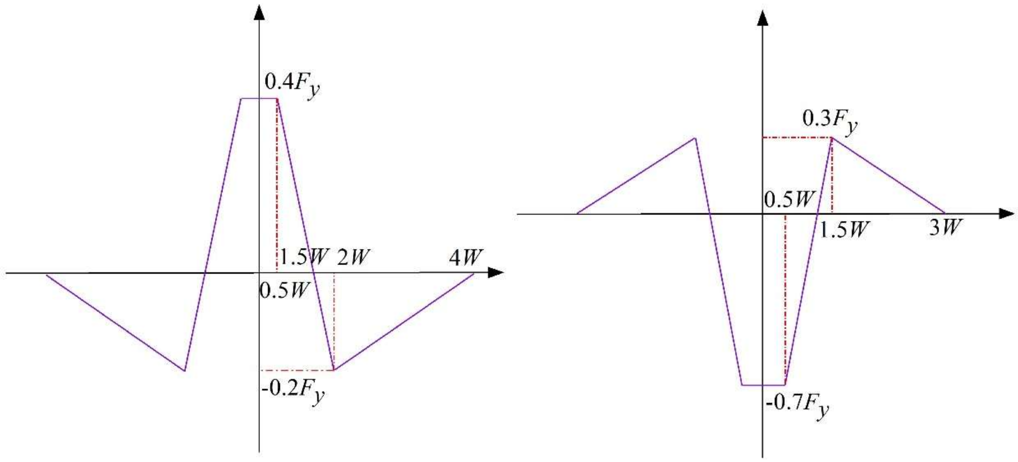

(a) Inner wall of steel pipe (b) Outer wall of steel pipe

Fig. 19. Axial residual stress simplification

3. Optimization of steel pipe welding process parameters based on numerical analysis

The experimental data were obtained by simulating 11 groups of parameters through ABAQUS, and the next step is to analyze the data to find the 6 parameter values that make the dependent variable smallest, to achieve the purpose of optimizing the welding parameters, the general idea is to use radial basis function (RBF) neural network to fit the sample data, to find the nonlinear mapping relationship between the independent variable and the response variable, and then to optimize the data with particle swarm algorithm (PSO) for optimization, to find out the set of independent variable parameter values that make the dependent variable the smallest, the overall data optimization process is shown in Figure 20.

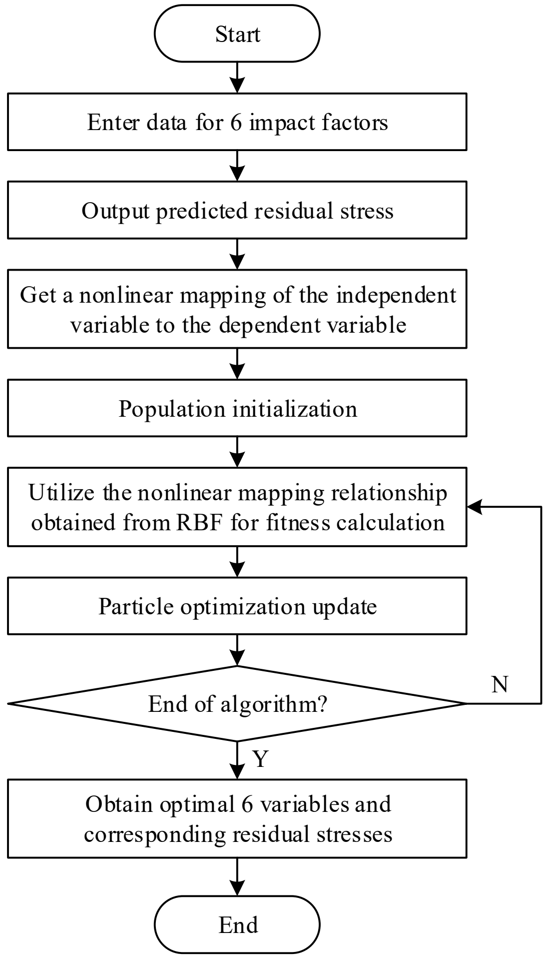

Fig. 20. Flowchart of overall data optimization

3.1. Modeling radial basis function neural network training

Radial basis function neural network (RBF) is a unique, efficient and stable feed-forward network model, which has the function of optimal approximation and overall optimization, and at the same time, the training method is also very fast and simple, there is no local optimization and other problems, the above advantages make the RBF network in the process of practice, and has gained a wide range of applications [24]. Radial basis function RBF is a class of hidden units of the "base" of the composition of the space, the input vector to carry out the corresponding transformation of the low-dimensional data information into the high-dimensional space, after the hidden units of the transmission of the weighted summation of the processing, the output value. The structure of the radial basis neural network is shown in Fig. 21. Its activation function is mainly utilized by the radial basis operator function, which is often defined as the Euclidean distance function from any point in the space, to a specific core. According to Fig. 21, the activation function of the radial basis neural network is based on the distance $\|dist\|$ between the vector and the weight vector as the independent variable. The equation for its activation operator function is as follows:

$$R\left(\|dist\|\right) = e^{-\|dist\|^2} \tag{43}$$

As the gap between the weights as well as the input vectors continues to decrease, the output of the network increases, and when the input vectors are aligned with the weight vectors, the neuron automatically outputs 1. In Fig. 21, b is the threshold value, which is used to control the sensitivity of the neuron.

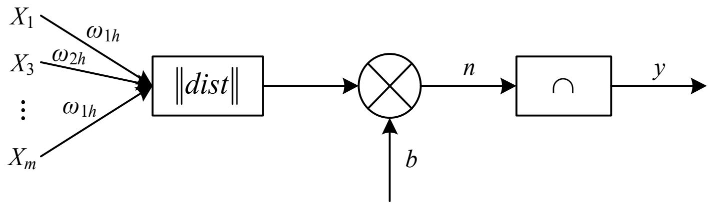

Fig. 21. Radial base neuron model

In this paper, 6 influencing factors are taken as input, and the maximum value of residual stress after welding is used as the output, the RBF neural network mapping model is constructed, the relationship between the 6 independent variables and the dependent variables is fitted, and the radial neural network is established by using $newrbe()$, the test data information is directly called from the data, the learning and testing are carried out, and the simulation is carried out by using $sim()$ operation functions, and all the 11 samples obtained through uniform experiments are used as training samples to fit the curve, and the RBF neural network fitting results are shown in Figure 22. As can be seen in Figure 22, the RBF neural network is able to fit the relationship between the six influences and the dependent variable very well, with a fitting error of almost zero.

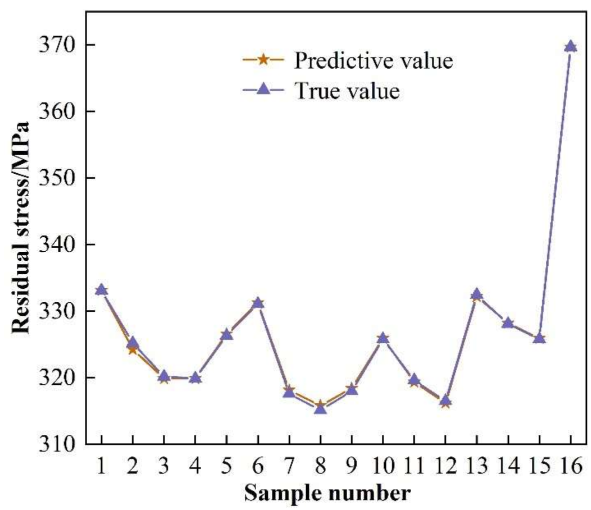

Fig. 22. Comparison of RBF neural network fitting results

In order to verify the accuracy of the RBF neural network fitting results, this paper additionally selects 16 groups of experimental data generated by random collocation of each test parameter as test samples to test the neural network obtained from training, and the sample test results are shown in Figure 23. The error of the step of testing the nonlinear mapping between the input and output of the sample is very small, which indicates that the method of this paper to get the RBF neural network fitting training samples through the method of uniform experimental design has a high training accuracy.

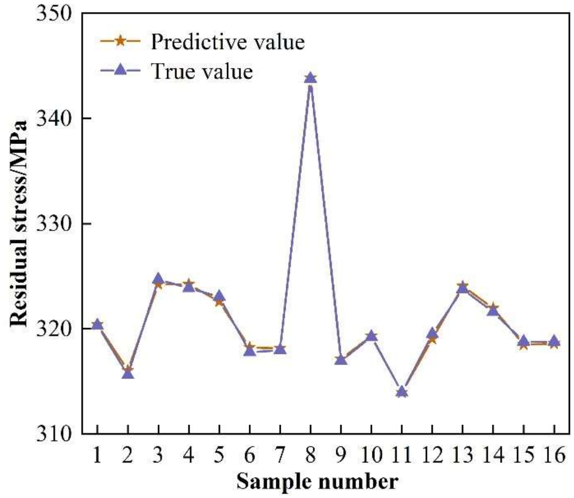

Fig. 23. Comparison of test sample effects

3.2. *Optimization using particle swarm algorithm*

Particle Swarm Algorithm (PSO) is a group intelligence optimization algorithm, the algorithm comes from the study and analysis of bird feeding activities, birds in the predation, the most simple and effective way to find food, is to search the current closest to the food of the bird around [25].PSO algorithms from the behavioral activities of this type of animal, to obtain the inspiration and will be used in the solution of the optimization problem of this idea.

A population consisting of a total of N particles is randomly initialized in the search space of n-dimensional feasible solutions. During the iteration of the algorithm, the state of any particle i in the population is determined by two quantities, i.e., the position and velocity of the particle, which are denoted as $X_i = \left(X_{i1}, X_{i2}, \cdots, X_{in}\right)^T$ and $V_i = \left(V_{i1}, V_{i2}, \cdots, V_{in}\right)^T$, respectively. In addition, any particle i updates its position and velocity during the iteration process based on the individual extreme value and the population extreme value, where the individual extreme value denotes the optimal position searched for so far by the ith particle, which is denoted as $P_i = \left(P_{i1}, P_{i2}, \cdots, P_{in}\right)^T$, and its fitness is p_{besti}, while the population extreme value denotes the optimal position searched for so far by all particles, which is denoted as $P_g = \left(P_{g1}, P_{g2}, \cdots, P_{gn}\right)^T$, and its fitness is g_{besti}. The formula for updating the velocity and position of a particle is:

$$V_{id}^{k+1} = \omega V_{id}^{k} + c_1 r_1 \left(P_{id}^{k} - X_{id}^{k}\right) + c_2 r_2 \left(P_{gd}^{k} - X_{id}^{k}\right) \tag{44}$$

$$X_{id}^{k+1} = X_{id}^{k} + V_{id}^{k+1} \tag{45}$$

In Eq. (44) and Eq. (45), i denotes the number of particles in the population, and k denotes the number of current iterations. ω is the inertia weight. c_1 and c_2 are the acceleration factors, which are usually taken as 2. r_1 and r_2 are random numbers distributed between $[0,1]$. V_{id}^{k} denotes the search speed of the ith particle at the kth iteration, and X_{id}^{k} denotes the position of the ith particle at the kth iteration, which is generally restricted to a certain interval $[-X_{\max}, X_{\max}]$, $[-V_{\max}, V_{\max}]$.

In each iteration, the adaptation value of each particle to obtain a new position is compared with the optimal position experienced by itself and the optimal position experienced by the whole particle swarm, and if it is superior, it is updated P_{best} or G_{best}. In this paper, the upper and lower bounds of each independent variable are taken as the maximum and minimum values of each group of samples, and the number of particles is set to be 15, and the maximum number of evolutions is 200, $c_1 = c_2 = 2.10$, and the inertia weights are set to be $\omega = 0.75$.

3.3. PSO algorithm optimization results and analysis

In order to facilitate the intuitive analysis of the optimization results of the PSO algorithm, the Pareto optimal boundary is extracted as shown in Fig. 24. It can be seen that, due to the complex nonlinear mapping relationship between the welding process parameters and the optimization objective, the distribution of the later Pareto optimal solution set shows signs of separation. For this reason it is necessary to analyze the two separated parts of the figure separately and compare them with each other to take the optimal value.

The Parcto optimal results clearly reveal the inconsistency between the two optimization objectives in this paper, where a decrease in the value of either optimization objective leads to an increase in the value of the other optimization objective. When the optimization objective of the temperature difference along the pipe wall thickness at the weld reaches the minimum value, corresponding to point A in the figure, it can be seen that the optimization objective of the maximum equivalent residual stress in the weld heat-affected zone is at the maximum value at this time. On the other hand, when the maximum equivalent residual stress in the weld heat-affected zone takes the minimum value, as shown at point D in the figure, another optimization objective is at the maximum value at this time.

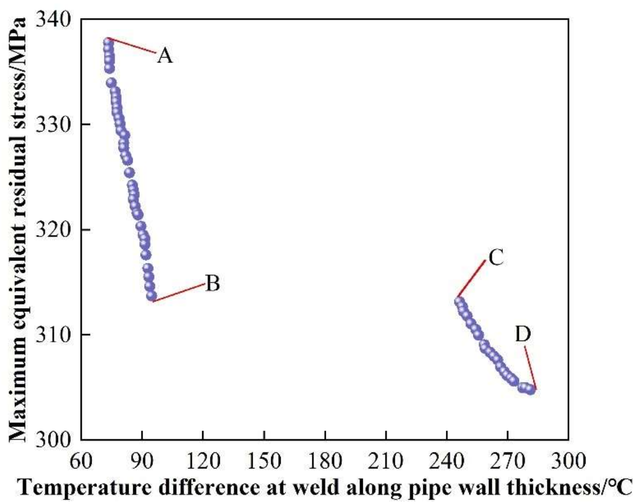

Fig. 24. Paleto optimal boundaries

The specific values corresponding to points A-D in Fig. 24 are shown in Table 1. From the AB section of the Pareto optimum boundary in Fig. 24, it can be seen that the maximum equivalent residual stress in the heat affected zone of the weld decreases as the temperature difference at the weld along the direction of the pipe wall thickness increases. And during the change from point A to B, the temperature difference at the weld along the pipe wall thickness increases from 73°C to 95°C, which is 28.9% higher, while the value of the maximum equivalent residual stress in the welded heat-affected zone decreases from 338 MPa to 314 MPa, which is 7.1% lower.

In order to make the two optimization objectives of temperature difference and equivalent residual stress value achieve relative minimum at the same time, then it is relatively reasonable to choose the objective value corresponding to point B. Similarly, for the CD section of the Pareto optimal boundary in Fig. 24, it is more appropriate to choose point C after the same trade-off. Comparing the values of point B and point C in Table 1, it can be seen against Fig. 24 that the vertical coordinate values of point B and point C are almost the same, while the horizontal coordinate value of point C is 246°C, which is 2.59 times that of point B, 95°C. Considering the above factors, this paper takes point B with smaller value of transverse coordinate as the final optimum point under this working condition, and its corresponding process parameters are the optimum process parameters in this paper.

Table 1. Extreme value points on Pareto boundary

Extremum point	Opening Angle /°	Current frequency /kHz	Distance from coil to V point /mm
A	5.00	218.34	281.00
B	5.00	220.58	264.00
C	3.85	213.47	264.00
D	3.52	216.87	264.00

The above analysis is carried out from the Pareto optimal boundary, and the optimal point is determined after comprehensive comparison, but it is difficult to comprehensively examine the information contained in the Pareto optimal solution set by this analysis alone, and the following analysis is carried out separately to analyze the effect of the three process parameters, namely, the opening angle, the current frequency, and the distance from the coil to the weld V point, on the two optimization objectives of the temperature difference and the maximum equivalent residual stress.

The effects of the opening angle on the two optimization objectives of temperature difference and maximum equivalent residual stress are shown in Figures 25 and 26, respectively. The data points are divided into two distinct parts. In the left part of the two figures, it can be seen that as the opening angle increases, the temperature difference along the pipe wall thickness at the weld decreases, while the maximum equivalent residual stress in the weld heat-affected zone increases, and there is a trend between the two. In the right part of the two figures, the opening angle is 5 °, which corresponds to the optimization target value in the two parts of the overall more acceptable. Therefore, the opening angle is taken as 5° after comprehensive comparison and analysis. In the Dianzhong water diversion project steel pipe welding process, the smaller the weld opening angle, the stronger the neighborhood effect, the larger the temperature difference corresponding to the possibility of welding defects, so the appropriate increase in the opening angle is conducive to improving the quality of welding.

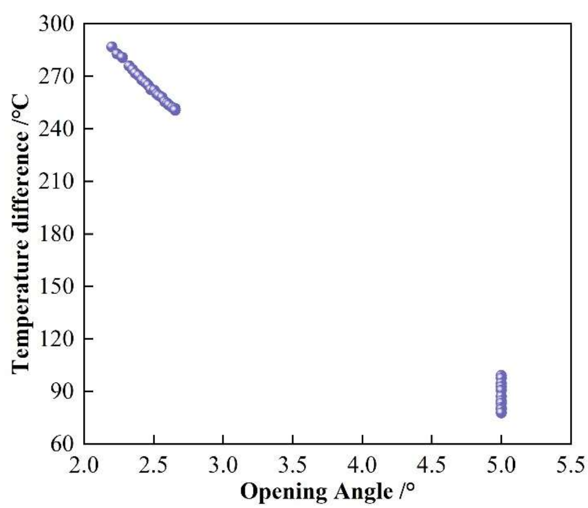

Fig. 25. The impact of the opening angle on the weld temperature difference

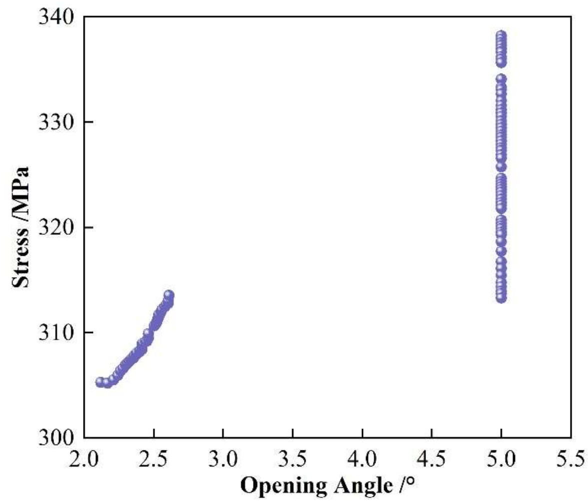

Fig. 26. The impact of the opening angle on the maximum equivalent residual stress of HAZ

The effect of current frequency on the two optimization objectives of this temperature difference and maximum equivalent residual stress is shown in Fig. 27 and Fig. 28, respectively, and the visible data points are similarly divided into two parts. In the left part of Fig. 27, the temperature difference along the pipe wall thickness at the weld is gradually increasing with the increase of current frequency, and its average value is 3.05 times of that in the right part (horizontal coordinate 215-220 kHz). In the left part of Fig. 28 (horizontal coordinate 211-215kHz), with the increase of current frequency, the maximum equivalent residual stress in the heat affected zone of the weld decreases gradually, and its value is lower than that of the right part of the figure, and when the current frequency is taken as 217.35kHz, the optimization target value in the corresponding two figures is relatively small. Therefore, the current frequency is taken as 217.35kHz.

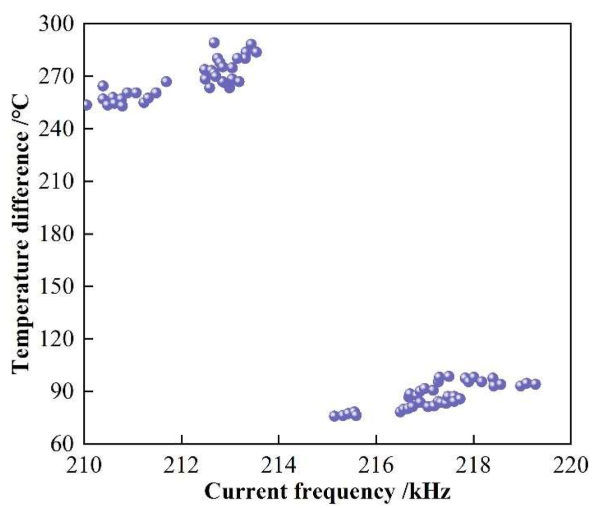

Fig. 27. The impact of current frequency on the weld temperature difference

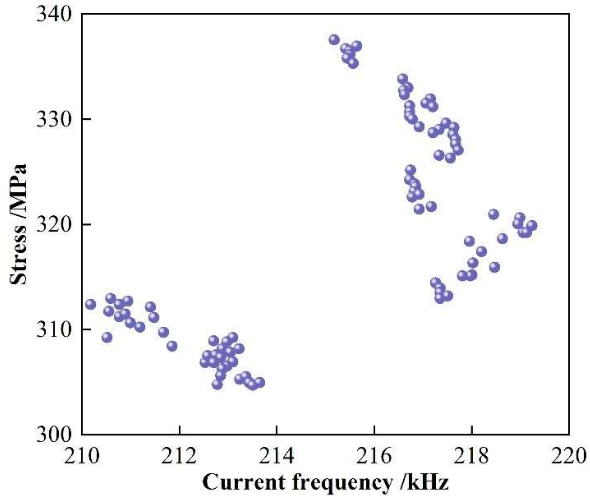

Fig. 28. The impact of current frequency on the maximum equivalent residual stress

The effects of the coil-to-weld V-point distance on the two optimization objectives of temperature difference and maximum equivalent residual stress are shown in Figs. 29 and 30, respectively, where the data points are similarly divided into two parts. When the coil to weld V point distance of 252mm, the two graphs corresponding to the target value of a relatively small value of the point, with the coil to weld V point distance increases, the temperature difference along the pipe wall thickness at the weld is slower to reduce the maximum equivalent residual stress of the weld heat-affected zone increased by a larger magnitude, so go to the coil distance from the weld V point of 252mm to make the two optimization objectives are relatively small.

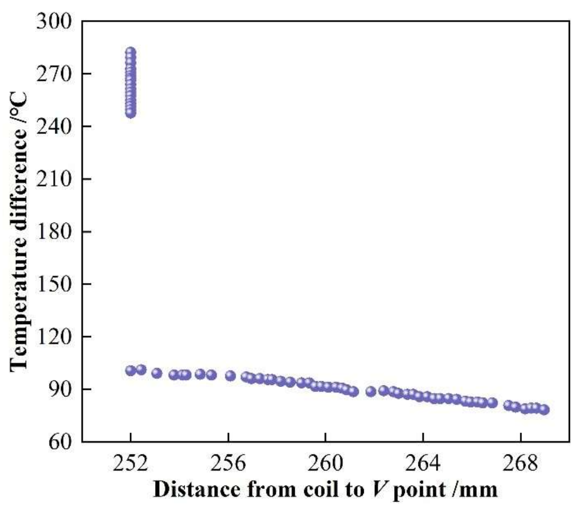

Fig. 29. The impact of the distance of coil to V point on the weld temperature difference

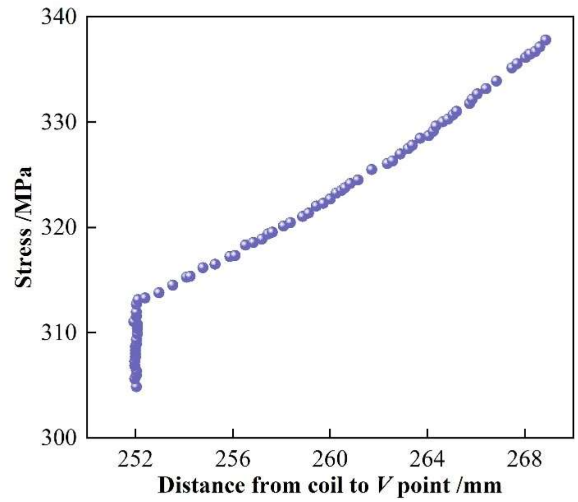

Fig. 30. The impact of the distance of coil to V point on the maximum stress

After the comprehensive analysis of each process parameter on the optimization objective, the optimal values of each process parameter for this condition are finally determined as the opening angle is taken as 5°, the current frequency is taken as 217.35 kHz and the coil distance from point V is 252 mm.

4. Conclusion

This paper combines the finite element analysis method and the displacement variational method to realize the simulation of the welding process of steel pipe in the Dianzhong water diversion project, and uses the radial basis function (RBF) neural network and the particle swarm algorithm (PSO) to realize the optimization of the parameters of the welding process of the steel pipe.

The simulation results show that the von mise equivalent stress reaches the nominal yield strength of the material in the weld region, the stress is close to zero in the parts away from the weld, and the von mise equivalent stress gradually transitions between the weld and the remote parts. Annular residual stress in the pipe wall is significantly different, in the pipe wall presents compressive stress, and the residual compressive stress is close to the yield strength of the material, and in the pipe wall presents tensile stress, residual tensile stress is close to 0.4 times the yield strength of the material. The distribution of axial residual stresses in the inner and outer walls of the steel pipe is also different, similar to the annular residual stresses, the same compressive stresses in the outer wall of the steel pipe, and the compressive stresses are close to 0.7 times the yield strength of the material, while the tensile residual stresses are presented in the inner wall of the steel pipe, and the quantity value is close to 0.3 times the yield strength of the material.

For the sample of Q420 steel used in this paper for steel pipe welding, a set of optimum process parameters were obtained, i.e., when the opening angle is 5°, the current frequency is 217.35 kHz, and the distance from the coil to the V-point is 252 mm, the optimization objective values corresponding to all are smaller and the weld quality of the weld seam is better.

Funding

This work was supported by science and technology research and development plan project of China Railway Group Limited (2020-major special projects-04).

References

[1] Chen, J., Yang, X., Dao, H., Gu, H., Chen, G., Mao, C., ... & Yan, Z. (2024). Analyses on Characteristics of Spatial

Distribution and Matching of the Human–Land–Water–Heat System on the Yunnan Plateau. Water, 16(6), 867.

[2] Jigqi, C. U. I., Shunchuan, W. U., CHENG, H., Tao, W. A. N. G., JIANG, G., Shijiang, P. U., & Zijian, R. E. N. (2024). Time series prediction of the surrounding rock displacement of a soft rock tunnel in the Central Yunnan Water Diversion Project. Journal of Tsinghua University (Science and Technology), 64(7), 1215-1225.

[3] HE, S. H., LAI, Y. Z., YE, F. Y., SHEN, C. Y., & PAN, F. (2022). Temporal and Spatial Variation of Water Vapor Transport over the Main Water-receiving Area of Water Diversion Project in Central Yunnan Province. Journal of Yangtze River Scientific Research Institute, 39(5), 36.

[4] Fu, P., Yin, J., Ding, X., & Liu, Y. (2020, October). Deformation-strain field characteristics and fault activities in central Yunnan water diversion project area. In IOP Conference Series: Earth and Environmental Science (Vol. 570, No. 6, p. 062029). IOP Publishing.

[5] Singh, R. (2020). Applied welding engineering: processes, codes, and standards. Butterworth-Heinemann.

[6] Sharma, H., Rajput, B., & Singh, R. P. (2020). A review paper on effect of input welding process parameters on structure and properties of weld in submerged arc welding process. Materials Today: Proceedings, 26, 1931-1935.

[7] Khan, M., Dewan, M. W., & Sarkar, M. Z. (2021). Effects of welding technique, filler metal and post-weld heat treatment on stainless steel and mild steel dissimilar welding joint. Journal of Manufacturing Processes, 64, 1307-1321.

[8] Pereira, A. B., & de Melo, F. J. (2020). Quality assessment and process management of welded joints in metal construction—A review. Metals, 10(1), 115.

[9] Rachmat, R. S., Anggraini, L., Sihotang, W., & Ameyama, K. (2022). Analysis of Welding Procedure Specifications for steel line pipe material. SINERGI, 26(3), 279-286.

[10] Papaefthymiou, S. (2021). Industrial Pipeline Welding. Welding Technology, 387-418.

[11] Favi, C., Campi, F., Germani, M., & Mandolini, M. (2019). A data framework for environmental assessment of metal arc welding processes and welded structures during the design phase. The International Journal of Advanced Manufacturing Technology, 105, 967-993.

[12] Prateepasen, A., & Aumpiem, A. (2021). Problems causing delays and risk factors in welding construction projects of Thailand. Engineering Journal, 25(5), 33-44.

[13] Lin, R., Feng, B., Liu, L., Yu, C., Huang, J., Wang, X., & Yang, M. (2023). Effect of welding inclination angle on strain distribution of X80 pipeline steel welded joint in mountain environment. Journal of Materials Engineering and Performance, 1-8.

[14] Kolawole, F. O., Kolawole, S. K., Agunsoye, J. O., Adebisi, J. A., Bello, S. A., & Hassan, S. B. (2018). Mitigation of corrosion problems in API 5L steel pipeline-a review. J. Mater. Environ. Sci, 9(8), 2397-2410.

[15] Yang, S. Y., Lin, J. M., Lin, W. Y., & Chang, C. W. (2018). Cancer risk assessment for occupational exposure to chromium and nickel in welding fumes from pipeline construction, pressure container manufacturing, and shipyard building in Taiwan. Journal of occupational health, 60(6), 515-524.

[16] Mehrifar, Y., Karimi Zeverdegani, S., Faraji, M., & Rismanchian, M. (2019). Risk assessment of welders exposure to the released contaminated gases in different types of welding processes in a steel industry. Health Scope, 7(4).

[17] Shin, Y. J., & You, W. J. (2020). Effects of welding time and electrical power on thermal characteristics of welding spatter for fire risk analysis. Energies, 13(24), 6502.

[18] Kang, C., Shi, C., Liu, Z., Liu, Z., Jiang, X., Chen, S., & Ma, C. (2020). Research on the optimization of welding

parameters in high-frequency induction welding pipeline. Journal of manufacturing processes, 59, 772-790.

[19] Sun, Y., & Cheng, Y. F. (2022). Hydrogen-induced degradation of high-strength steel pipeline welds: A critical review. Engineering Failure Analysis, 133, 105985.

[20] Jeremić, L., Petrovski, B., Đorđević, B., & Sedmak, S. (2020). Structural integrity assessment of welded pipeline designed with reduced safety. Tehnički vjesnik, 27(5), 1461-1466.

[21] Van Hoa Cao & Gyu Hyun Go. (2024). A novel approach to stability analysis of random soil-rock mixture slopes using finite element method in ABAQUS. Natural Hazards(15),14381-14407.

[22] Stannat Wilhelm & Vogler Alexander. (2025). Approximation of optimal feedback controls for stochastic reaction-diffusion equations. ESAIM: Control, Optimisation and Calculus of Variations.

[23] Tang Xi Ya, Liu Jie, He Jie & Xie Qun Dan. (2013). Approximate Analytical Method of Load-Settlement Relation for Composite Foundation with Lateral Restriction. Applied Mechanics and Materials(477-478),453-458.

[24] Edyta A. Bauer & Wojciech Jagusiak. (2025). Prediction of ketosis using radial basis function neural network in dairy cattle farming. Preventive Veterinary Medicine106410-106410.

[25] Dianelys Vega Ruiz, Cássio Scarpelli Cabral de Bragança, Bernardo Lopes Poncetti, Túlio Nogueira Bittencourt & Marcos Massao Futai. (2025). Structural damage detection for a small population of nominally equal beams using PSO-optimized Convolutional Neural Networks. Mechanical Systems and Signal Processing112276-112276.